Submitted to the
XXII International Symposium on Lepton-Photon Interactions at High Energy
30 June - 5 July, Uppsala, Sweden

Abstract: 296 **Session: QCD/HS**

Leading neutron p_T distributions in deep inelastic scattering and photoproduction at HERA

ZEUS Collaboration

Abstract

The production of energetic neutrons in ep collisions has been studied with the ZEUS detector at HERA. The neutrons were measured with a forward neutron calorimeter and tracker in a $44\,\mathrm{pb}^{-1}$ sample of inclusive deep inelastic scattering data, and a sub-sample of $7\,\mathrm{pb}^{-1}$ of inclusive photoproduction data. The neutron transverse-momentum distributions are compared to the predictions of models of pion exchange. The photoproduction data has a steeper p_T^2 distribution than deep inelastic scattering consistent with the expectation from absorption.

1 Introduction

In ep scattering at HERA, a significant fraction of events contains a baryon carrying a large fraction of the incoming proton energy [1–3]. The production mechanism of these low-transverse-momentum leading baryons is not completely understood. Although leading neutrons can result from the fragmentation of the proton remnant, exchange models (Fig. 1) give a better description of the data. In this picture, the incoming proton emits a virtual particle which scatters on the photon emitted from the beam electron. The outgoing baryon, of energy E_B, carries a fraction $x_L = E_B/E_p$ of the beam energy, while the exchanged particle participates in the process with energy $(1 - x_L)E_p$.

In particular, one-pion exchange is a significant contributor to leading neutron production for large x_L [1]. For such a process the cross section for the semi-inclusive reaction $ep \to eXn$ factorizes into two terms:

$$\frac{d^2\sigma(W^2, Q^2, x_L, t)}{dx_L dt} = f_{\pi/p}(x_L, t)\sigma_{\gamma^*\pi}((1 - x_L)W^2, Q^2)$$

where W is the center-of-mass energy of the virtual photon-proton system and t is the square of the four-momentum of the exchanged pion. The flux of virtual pions emitted by the proton is represented by $f_{\pi/p}$ and $\sigma_{\gamma^*\pi}$ is the cross section of the virtual photon and virtual pion interaction. If the cross section is assumed to be independent of t, the angular distribution of produced neutrons is completely determined by the flux factor.

Many parameterizations of the pion flux have been suggested in the literature [4–11]. They have the general form:

$$f_{\pi/p}(x_L, t) \propto \frac{-t}{(t - m_\pi^2)^2}(1 - x_L)^{\alpha(t)}F^2(x_L, t)$$

The power $\alpha(t)$ and the form factor $F(x_L, t)$ are model dependent with parameters extracted from low energy hadron-hadron scattering data. In terms of p_T, the pion virtuality is:

$$t = -\frac{p_T^2}{x_L} - \frac{(1 - x_L)(m_n^2 - m_p^2 x_L)}{x_L}$$

This paper presents measurements of the p_T distributions of leading neutrons. The results are compared to several exchange models with various choices of their parameters.

One implication of exchange models is vertex factorization, which predicts that the dependence of the cross section on the baryon variables will be independent of those at the lepton vertex. At the lepton vertex, the significant variable is Q^2, the virtuality of the exchanged photon. In order to test vertex factorization, events in photoproduction with a quasi-real photon ($Q^2 \approx 0$) are compared to deep inelastic scattering (DIS) events with Q^2 values greater than a few GeV^2.

In a one-pion-exchange model, neutron absorption can occur through rescattering on the photon [12,13]. Since the size of the virtual photon falls like Q^{-1}, more neutron rescattering would be expected for photoproduction than for DIS. The variation of the mean size of the n-π system as a function of x_L in exchange models leads to an x_L dependence of the absorption. Hence vertex factorization will be violated. Previous studies with leading neutrons [2] show a mild violation of vertex factorization with the expected increase of rate when going from photoproduction to DIS. Similar effects have been seen for leading protons [3]. A difference in neutron x_L spectra between photoproduction and DIS has been compared to the expectations of absorption models [14].

The present analysis compares the p_T distributions of leading neutrons as a function of x_L in photoproduction and DIS. In absorption models the connection to the p_T distributions is given by the n-π separation whose size is inversely proportional to p_T. Rescattering processes remove neutrons from small n-π systems hence with large p_T. Thus rescattering results in a depletion of neutrons at high p_T in photoproduction relative to DIS.

2 Detectors

A detailed description of the ZEUS detector can be found elsewhere [15]. A brief outline of the components that are most relevant for this analysis is given below.

The high-resolution uranium–scintillator calorimeter (CAL) [16] consists of three parts: the forward (FCAL), the barrel (BCAL) and the rear (RCAL) calorimeters. Each part is subdivided transversely into towers and longitudinally into one electromagnetic section (EMC) and either one (in RCAL) or two (in BCAL and FCAL) hadronic sections (HAC). The smallest subdivision of the calorimeter is called a cell. The CAL energy resolutions, as measured under test-beam conditions, are $\sigma(E)/E = 0.18/\sqrt{E}$ for electrons and $\sigma(E)/E = 0.35/\sqrt{E}$ for hadrons (E in GeV). The EMC sections were used to detect scattered positrons in DIS events and the RCAL was used to trigger on the dissociated photon in photoproduction events.

Bremsstrahlung $ep \to e\gamma p$ and the photoproduction of hadrons $ep \to eX$ are tagged using the luminosity (LUMI) detectors [17]. The bremsstrahlung photons are measured with a lead-scintillator calorimeter located $Z = -107\,\mathrm{m}$[1] from the interaction point in the positron-beam direction. A similar calorimeter at $Z = -35\,\mathrm{m}$ from the interaction point is used to measure positrons scattered at very small angles in an energy range 5-20 GeV, with an energy resolution of $0.19\sqrt{E}$ (E in GeV).

[1] The ZEUS coordinate system is a right-handed Cartesian system, with the Z axis pointing in the proton beam direction, referred to as the "forward direction", and the X axis pointing left towards the center of HERA. The coordinate origin is at the nominal interaction point.

The forward neutron calorimeter (FNC) [18–20] was installed in the HERA tunnel at $\theta = 0$ degrees and at $Z = 106\,\mathrm{m}$ from the interaction point in the proton-beam direction, as depicted in Fig. 2. It was used for the 1995-2000 data taking. The FNC is a lead-scintillator calorimeter with an energy resolution for hadrons of $\sigma_E/E = 0.70/\sqrt{E(\,\mathrm{GeV})}$. Three planes of veto counters were located in front of the FNC.

In the spring of 1998 a forward neutron tracker (FNT) was installed in the FNC at a depth of one interaction length. It is a scintillator hodoscope designed to measure the position of neutron showers. Each scintillator finger is 16.8 cm long, 1.1 cm wide and 0.5 cm deep: 17 are used for X position reconstruction and 15 for Y. Figure 3 shows the position of the FNT hodoscope in the FNC relative to the incoming neutron beam. The irregular outlined area shows the geometric acceptance defined by magnet apertures. This limits detection to neutrons with production angles less than 0.75 mrad, allowing transverse momenta in the range $p_T \leq E_n\theta_{\max} = 0.69x_L\,\mathrm{GeV}$. The allowed kinematic regions in p_T^2 and t are shown in Fig. 4. Scans by a ^{60}Co radioactive source were performed to calibrate and monitor both detectors.

The position resolution of neutron showers in the FNT of $\pm 0.23\,\mathrm{cm}$ was measured by placing an adjustable collimator in front of the outermost veto counter of the FNC during special test and calibration runs.

3 Data selection and analysis

The data for this analysis were collected in 2000 when HERA collided 27.5 GeV positrons with 920 GeV protons. Separate triggers were used to collect DIS and photoproduction events with leading neutrons.

The DIS events were collected using a trigger that detected the scattered electron in the CAL. In the offline analysis, the scattered electron was required to be at least 3 cm from the inner edge of the beam-pipe hole in the RCAL. This limited the acceptance to the kinematic range $Q^2 > 2\,\mathrm{GeV}^2$ with an average Q^2 value of $\langle Q^2\rangle \simeq 7.8\,\mathrm{GeV}$. The integrated luminosity of the DIS sample was $43.6\,\mathrm{pb}^{-1}$.

The photoproduction events were collected during the last part of the 2000 running period using a trigger that required at least 5 GeV in the positron tagger in coincidence with at least 464 MeV in the RCAL EMC. The acceptance of the positron tagger limited the photon virtuality to $Q^2 < 0.02\,\mathrm{GeV}^2$, with a median Q^2 of approximately $\langle Q^2\rangle \simeq 5 \times 10^{-5}\,\mathrm{GeV}^2$. Offline, events were required to have less than 1 GeV in the photon tagger to reject overlapping bremsstrahlung events. The integrated luminosity of the photoproduction sample was $6.7\,\mathrm{pb}^{-1}$.

Both triggers required at least 165 GeV of energy to be deposited in the FNC. Offline cuts were used to select clean neutron candidates, and further cuts were applied to select neutrons with a well reconstructed position.

Figure 5 shows a scatter plot of reconstructed hits in the FNT. The irregular curve is the aperture expected from a Monte Carlo simulation of the beam line. The simulation also models significant amounts of dead material in some regions of the aperture. There is good agreement between the simulation and the data distribution. For example, the deficit of events observed around $Y \sim 10.5$ cm is well reproduced by the simulation of dead material. The energy resolution of the FNC, the position resolution of the FNT, and the inherent p_T-spread in the HERA proton beam are also simulated. The latter corresponds to a smearing of the zero-degree point by 0.45 cm horizontally and 1.0 cm vertically, significantly larger than the FNT resolution.

Reconstruction of the neutron scattering angle θ_n requires knowledge of the zero-degree point. By passing a symmetric distribution of neutrons through the simulation and fitting to the data, this point was determined to an accuracy of ± 0.2 cm in X and Y. This uncertainty is included in the systematic uncertainties on the p_T^2 distributions. Other significant contributions to the uncertainties are the FNC energy scale uncertainty of $\pm 2\%$ and the uncertainties in the dead material map.

4 Neutron p_T^2 distributions

The corrected p_T^2 distributions in DIS for different x_L bins are shown in Figs. 6 and 7. They are presented as normalized doubly differential distributions $(1/N_{\rm DIS})d^2N/dx_L dp_T^2$, where $N_{\rm DIS}$ is the number of DIS events without a neutron requirement. The aperture limitation $\theta_n < 0.75$ mrad is seen in the varying p_T^2 ranges plotted. The line on each plot is a fit to the functional form $dN/dp_T^2 \propto \exp(-bp_T^2)$, which gives a good description of the data. The dependence of the slopes b on x_L is shown in Fig. 8. Below $x_L = 0.3$ they are consistent with zero; they rise linearly in the range $0.3 < x_L < 0.85$ to a value of $b \simeq 8\,{\rm GeV}^{-2}$, and then decrease slightly at higher x_L. The systematic uncertainties, which are highly correlated, are shown by the shaded band in Fig. 8.

The slopes can be compared to parameterizations of the pion flux $f_{\pi/p}$. Although $f_{\pi/p}$ is not an exponential in p_T^2, at fixed x_L the models can be fit to the form $\exp(-bp_T^2)$ and the resulting $b(x_L)$ values compared to the data. The results are shown in Fig. 9. Although one-pion exchange is expected to dominate neutron production only for $x_L > 0.6$–0.7, several of the models can be rejected immediately as the sole mechanism for producing leading neutrons. The data can also constrain the choice of parameters in some models.

For example, the curves labeled Bishari-0, Bishari-4 [4], and KPP [5] are the same model with different choices of parameters. Bishari-4 is clearly inconsistent with the data.

To minimize effects of energy calibration and beam position drifts, only the subset of DIS data collected simultaneously with the photoproduction data are used for comparisons between the two sets. The p_T^2 distributions for both samples, normalized to unity at $p_T^2 = 0$, are shown in Fig. 10. The photoproduction distributions are clearly steeper in the range $0.6 < x_L < 0.9$. The difference of the slopes $\Delta b = b(Q^2 < 0.02\,\mathrm{GeV}^2) - b(Q^2 > 2\,\mathrm{GeV}^2)$ is less sensitive to systematic effects than each of the individual slopes. These values are plotted in Fig. 11. Within the systematic uncertainties the slopes for photoproduction are clearly larger in the range $0.6 < x_L < 0.9$, with $\Delta b = 0.5$–1.0 GeV^{-2}. The depletion of neutrons at large p_T^2 is qualitatively consistent with the expectations from absorption models.

5 Conclusions

The transverse-momentum distributions of leading neutrons in photoproduction and DIS events at HERA have been measured as a function of x_L. The p_T^2 distributions are well described by an exponential $\exp(-bp_T^2)$. The slope b rises linearly with x_L in the range $0.3 < x_L < 0.85$ for both photoproduction and DIS. The b values of photoproduction lie above the DIS values in the range $0.6 < x_L < 0.9$, which is consistent with the expectations from absorption models. The measured $b(x_L)$ dependence has been compared with various exchange models. For one-pion exchange, some models are inconsistent with the data, while the parameters of others are constrained by the data.

References

[1] ZEUS Coll., M. Derrick et al., Phys. Lett. **B 384**, 388 (1995);
H1 Coll., C. Adloff et al., Eur. Phys. J. **C 6**, 587 (1999);
ZEUS Coll., J. Breitweg et al., Nucl. Phys. **B 596**, 3 (2000).

[2] ZEUS Coll., J. Breitweg et al., Nucl. Phys. **B 637**, 3 (2003).

[3] H1 Coll., C. Adloff et al., Nucl. Phys. **B 619**, 3 (2001);
ZEUS Coll., J. Breitweg et al., Nucl. Phys. **B 658**, 3 (2003).

[4] M. Bishari, Phys. Lett. **B 38**, 510 (1972).

[5] B. Kopeliovich, B. Povh and I. Potashnikova, Z. Phys. **C 73**, 125 (1996).

[6] N.N. Nikolaev et al., Phys. Rev. **D 60**, 014004 (1999).

[7] L.L. Frankfurt, L. Mankiewicz and M.I. Strikman, Z. Phys. **A 334**, 343 (1989).

[8] K. Golec-Biernat, J. Kwiecinski and A. Szczurek, Phys. Rev. **D 56**, 3955 (1997).

[9] M. Przybycien, A. Szczurek and G. Ingelman, Z. Phys. **C 74**, 509 (1997).

[10] A. Szczurek, N.N. Nikolaev and J. Speth, Phys. Lett. **B 427**, 383 (1998).

[11] W. Melnitchouk, J. Speth and A.W. Thomas, Phys. Rev. **D 59**, 014033 (1998).

[12] N.N. Nikolaev, J. Speth and B.G. Zakharov, Preprint KFA-IKP(TH)-1997-17 (hep-ph/9708290), KFA-IKP, 1997.

[13] U. D'Alesio and H.J. Pirner, Eur. Phys. J. **A 7**, 109 (2000).

[14] ZEUS Coll.. Paper 824, XXXI International Conference on High Energy Physics, Amsterdam, Netherlands, 2002.

[15] ZEUS Coll., U. Holm (ed.), *The ZEUS Detector*. Status Report (unpublished), DESY (1993), available on `http://www-zeus.desy.de/bluebook/bluebook.html`.

[16] M. Derrick et al., Nucl. Inst. Meth. **A 309**, 77 (1991);
A. Andresen et al., Nucl. Inst. Meth. **A 309**, 101 (1991);
A. Caldwell et al., Nucl. Inst. Meth. **A 321**, 356 (1992);
A. Bernstein et al., Nucl. Inst. Meth. **A 336**, 23 (1993).

[17] J. Andruszków et al., Preprint DESY-92-066, DESY, 1992;
ZEUS Coll., M. Derrick et al., Z. Phys. **C 63**, 391 (1994);
J. Andruszków et al., Acta Phys. Pol. **B 32**, 2025 (2001).

[18] S. Bhadra et al., Nucl. Inst. Meth. **A 354**, 479 (1995).

[19] ZEUS Coll., FNC group, S. Bhadra et al., Nucl. Inst. Meth. **A 394**, 121 (1997).

[20] ZEUS FNC Group, S. Bhadra et al., *Proc. of the Seventh International Conference on calorimetry in High Energy Physics, Tuscon, Arizona, November 1997*, E. Cheu et al. (ed.), p. 295. World Scientific, Singapore (1998).

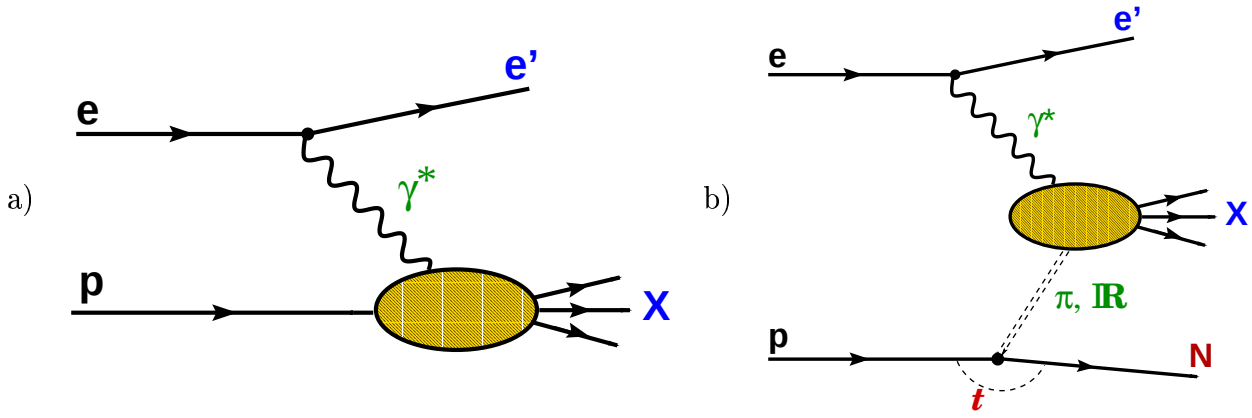

Figure 1: *a) HERA ep scattering event with the final-state baryon in the proton-fragmentation system, X. b) Leading baryon production via an exchange process.*

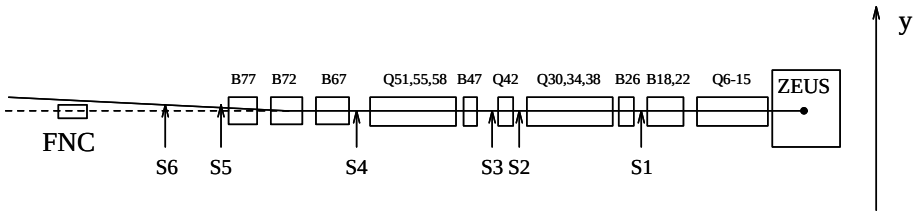

Figure 2: *The proton beamline downstream from the ZEUS interaction region. The proton beam is bent upward by approximately 6 mrad by the dipole magnets B67–B77 near Z=+70 m. The FNC is located on the zero-degree line at Z=+105.5 m. S1–S6 show the locations of the ZEUS Leading Proton Spectrometer.*

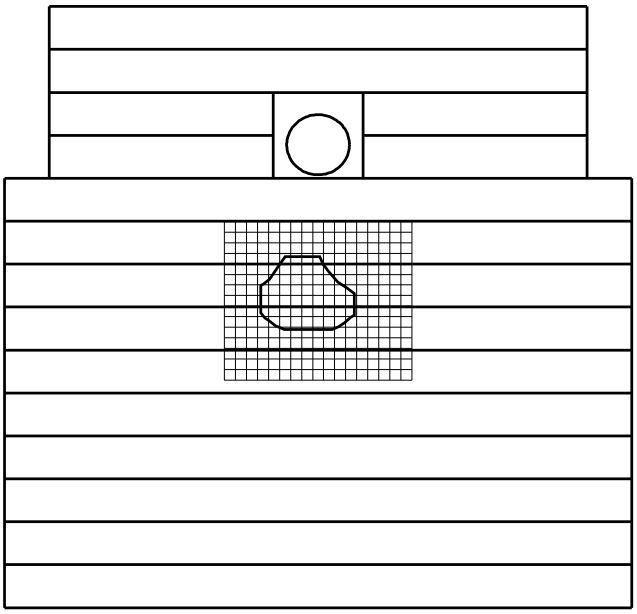

Figure 3: *Diagram of the FNC/FNT assembly. The heavy lines show the 5 cm vertical segmentation of the front part of the FNC. The hole through the third and fourth towers from the top allows the proton beam to pass through the calorimeter. The* 17×15 *grid of small squares shows the fingers of the FNT hodoscopes. The irregular curve shows the geometric aperture defined by upstream beamline elements, and the darkened square shows the zero-degree point.*

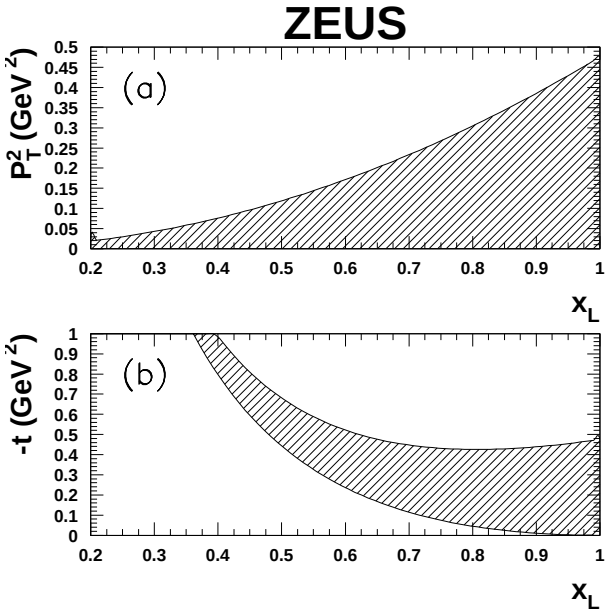

Figure 4: *The kinematic regions in (a)* p_T^2 *and (b)* t *covered by the angular acceptance of the FNC (*$\theta_n < 0.75$ *mrad) are shown as shaded bands.*

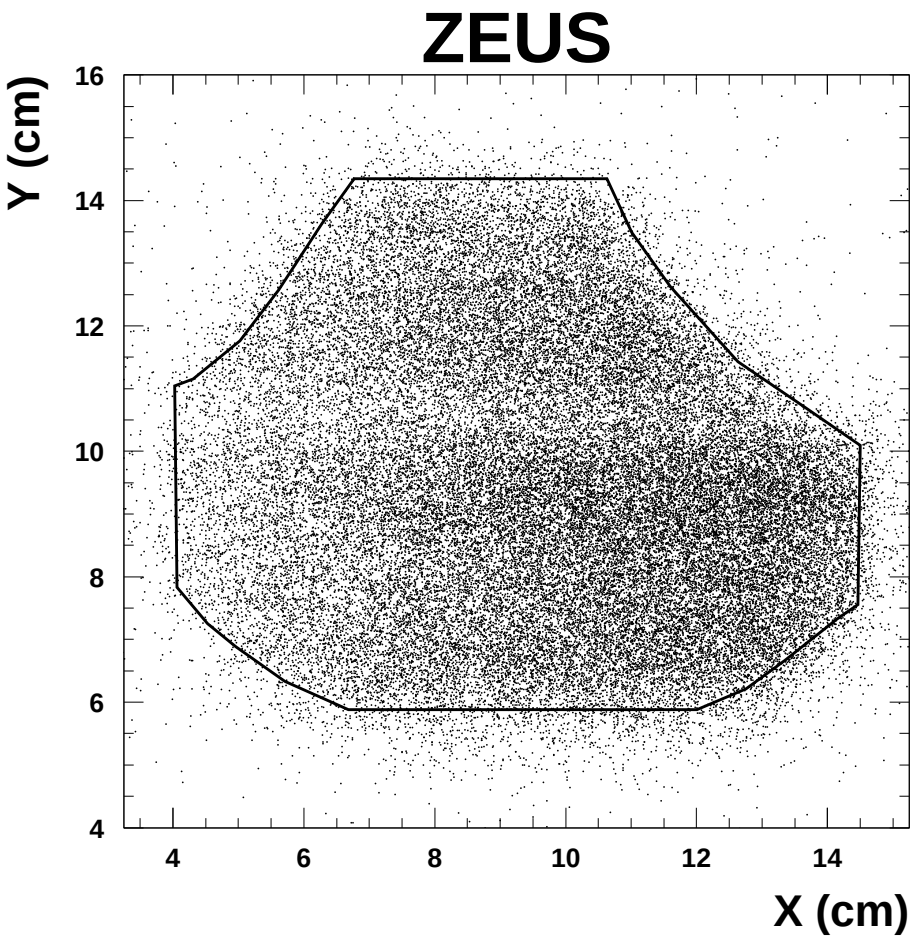

Figure 5: *Scatter plot of hits in the FNT. The irregular curve is the geometric aperture defined by upstream beamline elements as modeled in the Monte Carlo. The zero-degree point is at* $X = 12.5$ *cm,* $Y = 8.3$ *cm.*

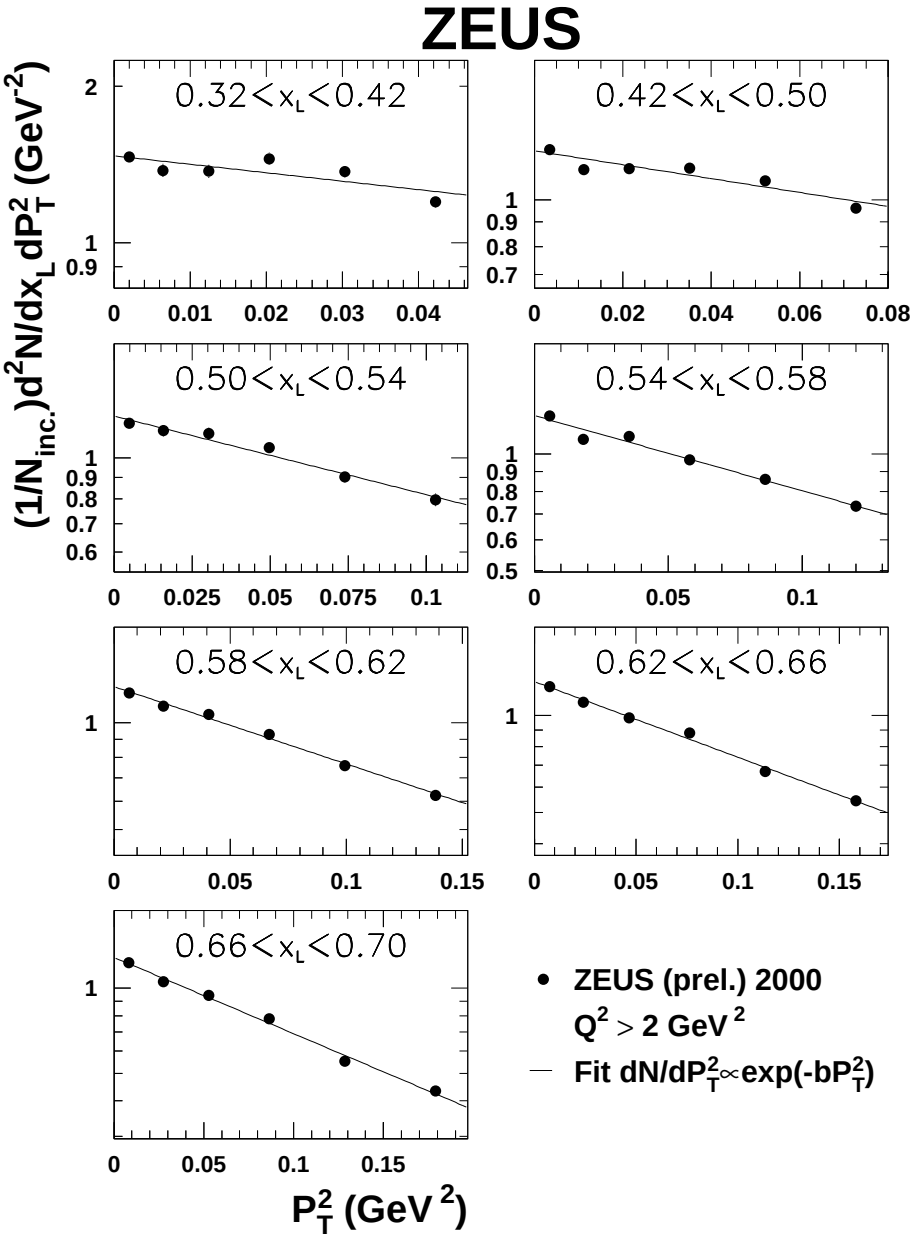

Figure 6: *The p_T^2 distributions for DIS for the low x_L bins. Note the logarithmic vertical scale and the varying p_T^2 ranges. The statistical errors are shown by a vertical error bar; in most cases they are smaller than the plotted symbol. The line on each plot is the result of a fit to the form $dN/dp_T^2 \propto \exp(-bp_T^2)$.*

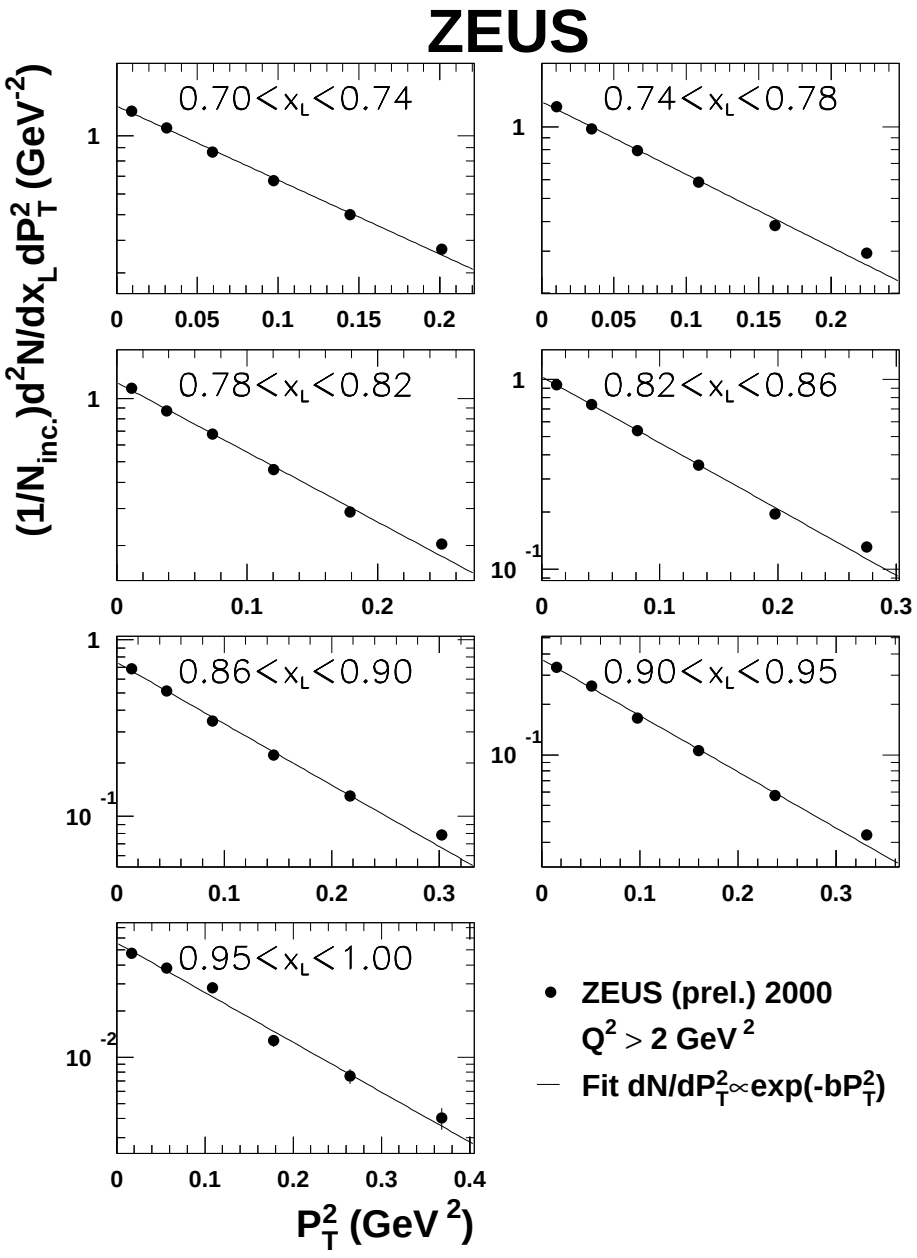

Figure 7: *The p_T^2 distributions for DIS for the high x_L bins. Note the logarithmic vertical scale and the varying p_T^2 ranges. The statistical errors are shown by a vertical error bar; in most cases they are smaller than the plotted symbol. The line on each plot is the result of a fit to the form $dN/dp_T^2 \propto \exp(-bp_T^2)$.*

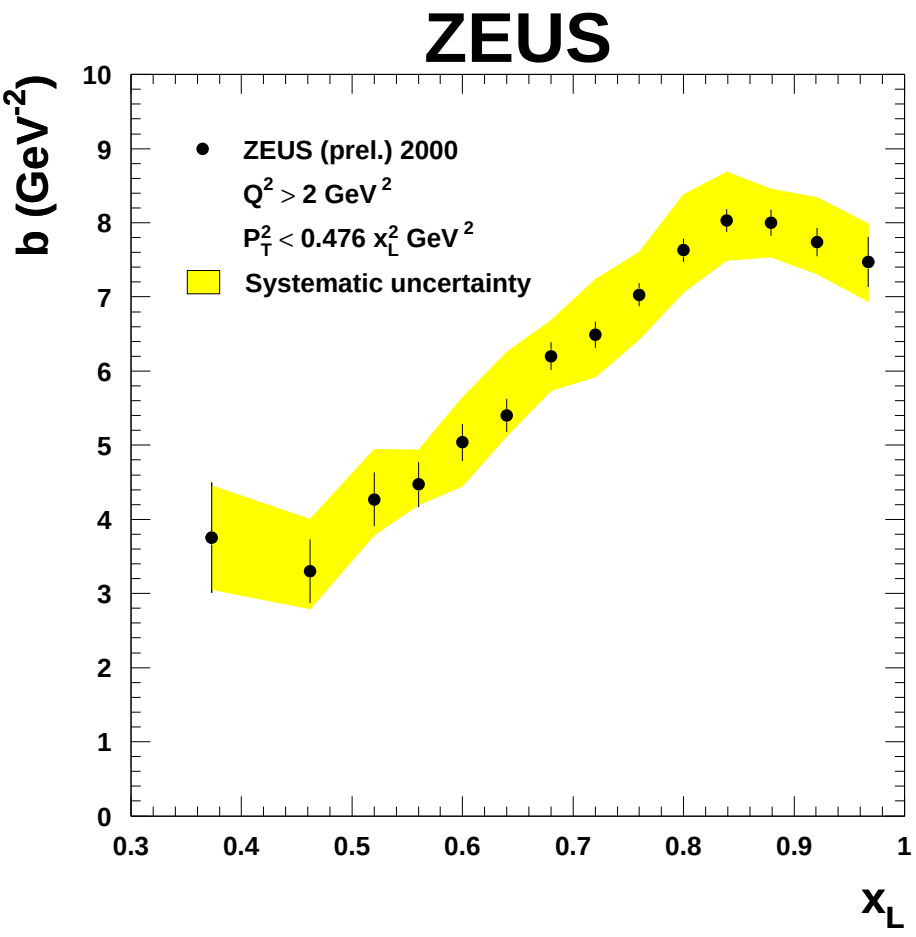

Figure 8: *The slopes b versus x_L from fits of the p_T^2 distributions in DIS to the form $dN/dp_T^2 \propto \exp(-bp_T^2)$ over the p_T^2 ranges shown in Figs. 6 and 7. The error bars show the statistical uncertainties; the shaded band shows the systematic uncertainties.*

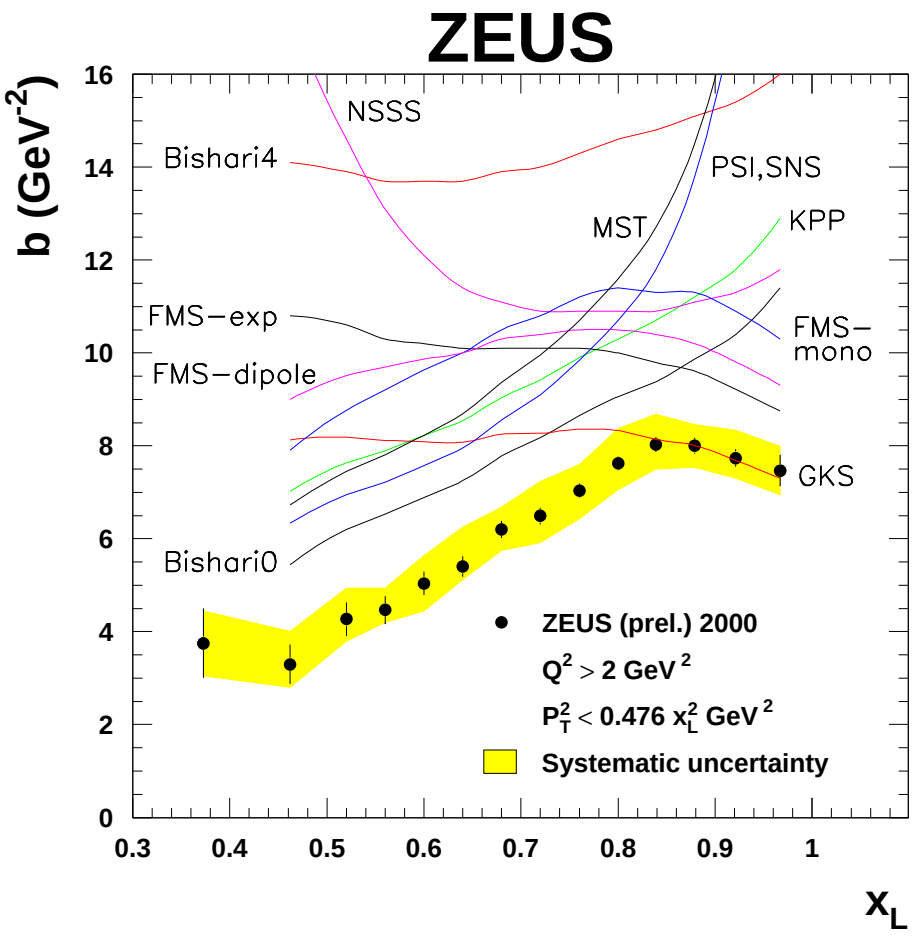

Figure 9: *The measured slopes b compared to the predictions of models of one-pion exchange alone. The curves are labeled by the authors' name or initials.*

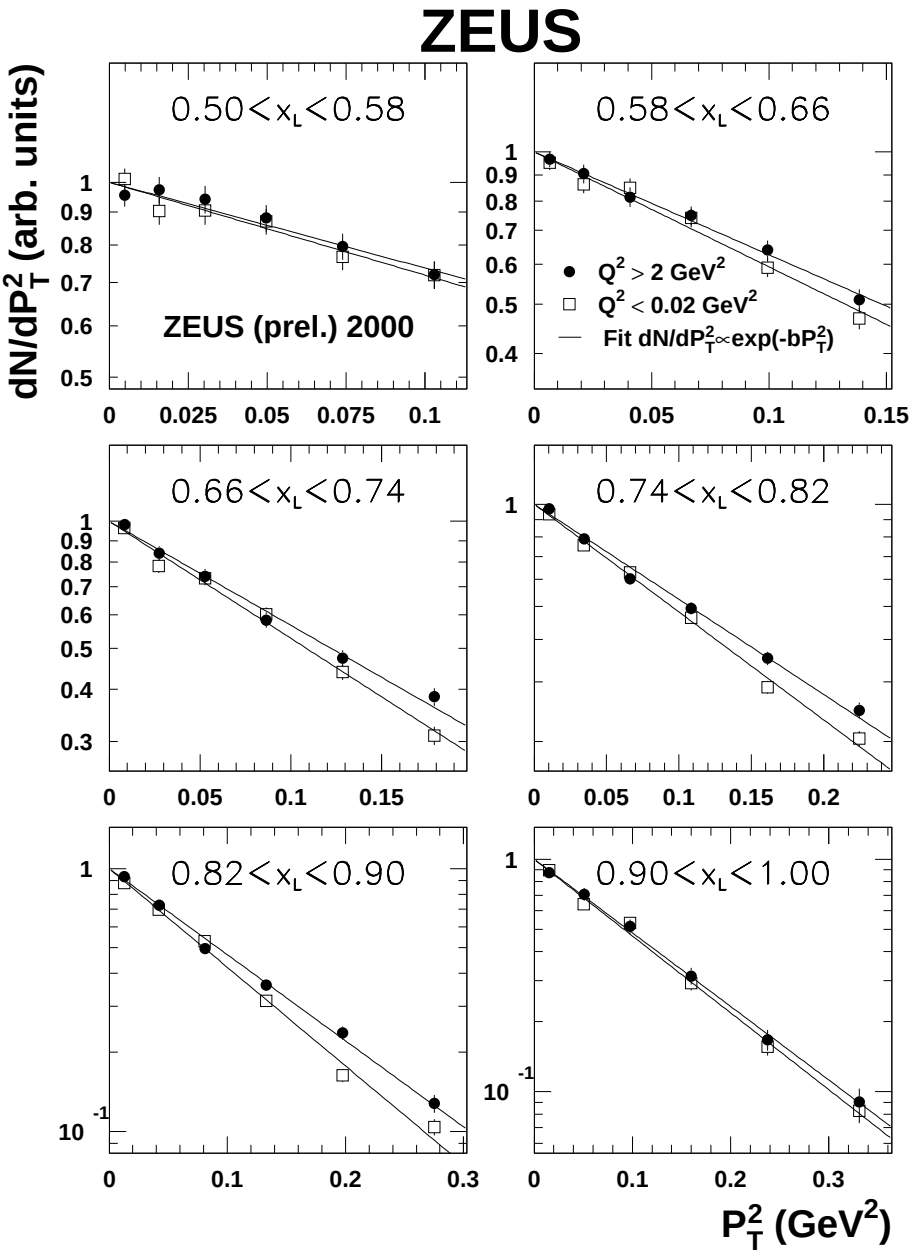

Figure 10: *The p_T^2 distributions for photoproduction and DIS. They are each normalized to unity at $p_T^2 = 0$. Note the logarithmic vertical scale and the varying p_T^2 ranges. The statistical errors are shown by a vertical error bar; in some cases they are smaller than the plotted symbol. The lines on each plot are the results of fits to the form $dN/dp_T^2 \propto \exp(-bp_T^2)$.*

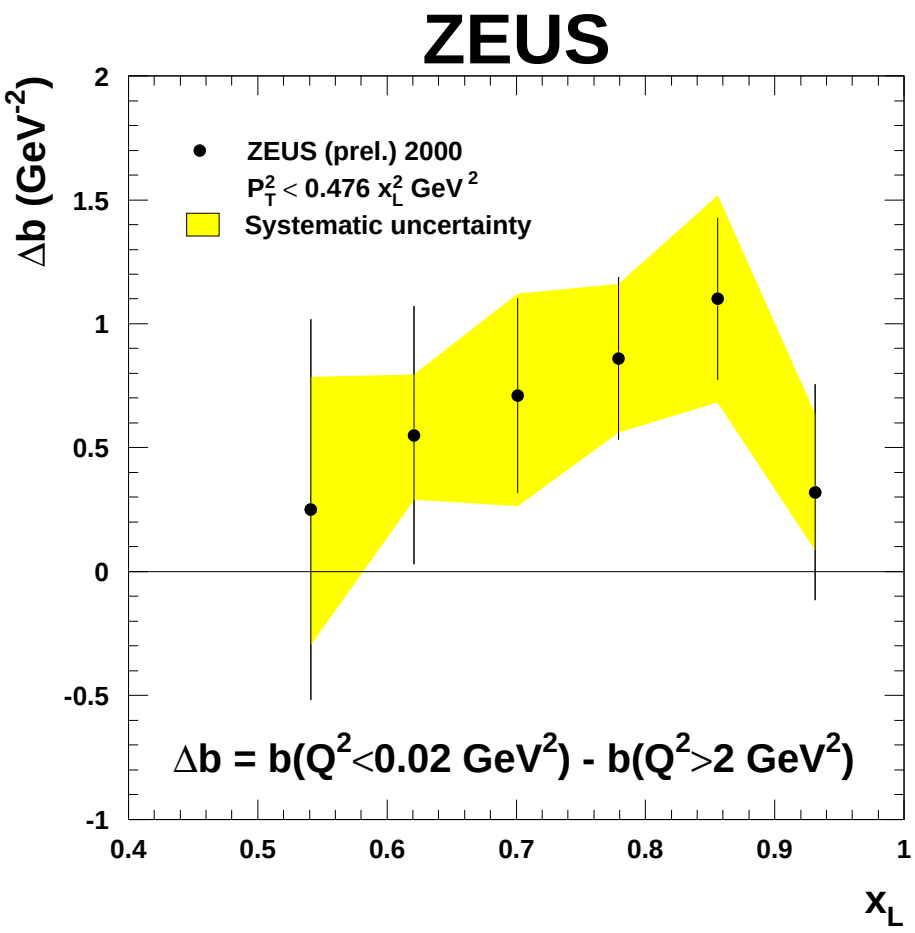

Figure 11: *The differences between slopes in photoproduction and DIS Δb versus x_L. The error bars show the statistical uncertainties; the shaded band shows the systematic uncertainties.*